Geometry optimization of a Lorentz force, resonating MEMS magnetometer

M. Bagherinia [a], M. Bruggi [a], A. Corigliano [a,*], S. Mariani [a], E. Lasalandra [b]

[a] Politecnico di Milano, Dipartimento di Ingegneria Civile e Ambientale, Piazza Leonardo da Vinci 32, 20133 Milano, Italy
[b] STMicroelectronics, AMS Group, Via Tolomeo 1, 20010 Cornaredo, Italy

1. Introduction

Lorentz force MEMS magnetometers are currently being studied for navigation systems and for the creation of multi-axis integrated microsystems, see e.g. [1–5] among recent publications. Devices based on Lorentz force appear to be particularly promising for the measurement of magnetic fields in the direction orthogonal to the substrate (z-axis magnetometers). With respect to the more diffused Hall effect sensors, Lorentz-force devices have the advantage of lower power consumption and easier integration with standard, silicon-based, MEMS fabrication technologies [3].

The authors research group has recently worked on various issues related to the design and fabrication of Lorentz force magnetometers in an industrial technology platform. In [5] design criteria have been discussed, mainly focused on the important problem of carefully evaluating the fluid-damping caused by the interaction of vibrating beams with the surrounding gas.

The purpose of the present paper is to discuss preliminary results concerning the application of efficient topology optimization techniques to the design of Lorentz-force magnetometers. A multi-physics approach is proposed for the optimal design of a polysilicon microsystem, which exploits the interaction between an AC input and the earth magnetic field to keep a compliant part (a clamped–clamped beam) into vibration. In the study, account is taken of coupling terms arising from: the Joule effect-induced temperature raise caused by the current flowing in the beam; the thermal-induced buckling effects on the stiffness of the beam; the Lorentz electromagnetic force acting on the beam due to the magnetic field; the electrostatic force due to parallel plate sensing.

Through appropriate simplifying assumptions, it is shown that the equations governing the dynamics of the beam can be recast in the typical form for a damped Duffing oscillator [6], where damping is caused by the fluid surrounding the oscillating body. The geometry of the beam is then optimized through a hybrid approach, maximizing the sensitivity of the MEMS to the magnetic field and minimizing its power consumption, keeping also its resonance frequency at a target value.

The paper is organized as follows: in Section 2 the multi-physics model of a beam subject to Lorentz force and electro-thermo-mechanical loading is described; Section 3 is dedicated to a brief description of topology optimization applied to the present multi-physics problem; results are discussed in Section 4, while closing remarks are given in Section 5.

2. Modeling of a resonating beam-like magnetometer

A SEM image of part of the resonating structure of the MEMS magnetometer here studied is reported in Fig. 1. This geometry has been devised to sense the earth magnetic field aligned with

---

* Corresponding author. Tel.: +39 0223994244; fax: +39 0223994300.
E-mail address: alberto.corigliano@polimi.it (A. Corigliano).
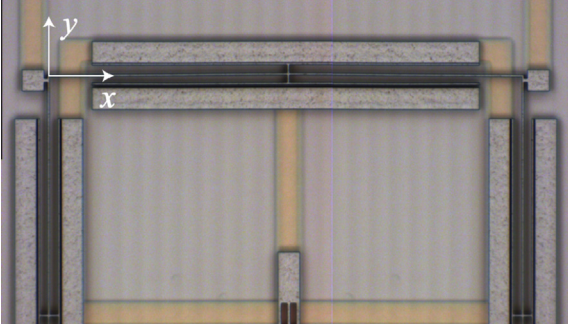
Fig. 1. Detail of the studied Lorentz-force MEMS magnetometer, and adopted reference frame.

the out-of-plane direction, orthogonal to the substrate surface (along axis z, according to the reference frame of Fig. 1). The whole system is characterized by four beams, all excited by the Lorentz force resulting from the interaction between the current flowing along the longitudinal axes of the beams themselves and the magnetic field. Sensing is achieved through a couple of parallel plates attached to the mid-span cross-section of each beam. Due to symmetry, all the beams in-plane resonate at the same frequency (or within a range of frequencies tuned by stochastic effects at the sub-micron length-scale). Anchors are placed at the four vertices of the mechanical system, so as current flow, symmetry of the structure and differential sensing are exploited to achieve mechanical cancelation of acceleration effects.

In this section we focus on a single beam Ω, featuring length L and constant cross-section of area A (with $A = bh$, b being the out-of-plane thickness and h the in-plane width). The beam is assumed in a clamped–clamped configuration, with displacements and rotations fully constrained at both its final cross-sections.

The dynamics of the beam in response to the external actions is formulated by considering the electro-thermo-mechanical coupling as a weak one: the elastic properties of the polysilicon film constituting the vibrating beam are independent of the electric and thermal fields, due to their relatively small amplitudes. Moreover, possible dissipation phenomena in the structure, like the thermo-elastic one [7], are assumed to provide a negligible effect on the investigated working conditions (see the discussion to follow). On the other hand, Joule effect gives rise to an increase of the temperature in the beam, which is fully accounted for as it can lead to a change of the resonance frequency. Finally, no eddy currents are assumed to develop inside and around the beam; the earth magnetic field hence forces the beam vibrations through the relevant Lorentz force effect.

The elastic response of the beam is modeled according to second-order theory, so as to allow for lateral deflections small in amplitude but indeed affecting the equilibrium state. In the orthonormal reference frame depicted in Fig. 1, dynamic equilibrium is enforced in weak form through (see also [8,9]):

$$\int_0^L \delta v'' EI v'' \, \mathrm{d}x + \int_0^L \delta v \eta \ddot{v} \, \mathrm{d}x - \int_0^L \delta v' P v' \, \mathrm{d}x - \int_0^L \delta v f \, \mathrm{d}x = 0 \qquad (1)$$

where according to the Bernoulli–Euler kinematics, shear deformations have been disregarded as target system geometries are characterized by high slenderness values. In Eq. (1): δv stands for the variation of field v; x is the longitudinal axis of the beam, whereas lateral displacements $v(x, t)$, where t is time, take place along axis y only; $v' = \partial v/\partial x$ and $v'' = \partial^2 v/\partial x^2$ respectively represent the rotation and the curvature of the beam axis; $\ddot{v} = \partial^2 v/\partial t^2$ represents instead the lateral acceleration field along the beam axis; E is the effective Young's modulus of the beam material in the longitudinal

direction (as the beam is made of polysilicon, we assume that its length L and cross-section area A allow adopting homogenized properties for the film); I is the cross-section moment of inertia of the beam about the out-of-plane z axis, so as EI is the flexural rigidity of the beam relevant to the modeled in-plane bending dominated vibrations; η is the mass per unit length of the beam (i.e. $\eta = \rho A$, ρ being the mass density of the material); P is the axial compressive load, to be considered as a state of residual stress due to the electro-thermo-mechanical coupling; f is the magnitude of the lateral load per unit length, provided by the external actions. The first two terms in Eq. (1) therefore represent the small displacement elastic (deformation) and kinetic (inertial) contributions; as already stated before, viscous dissipation is assumed instead to provide a negligible contribution to the dynamics of the beam alone.

If the beam is axially unstressed in the configuration at rest, P is induced by Joule effect. Because of the current i, flowing in the beam along its longitudinal axis, the temperature raise is given by conduction in a one-dimensional heat transfer mechanism, whereas convection is neglected due to the very low working pressure. Accordingly:

$$\Delta T(x) = 4 \Delta T_m \left[\left(\frac{x}{L} \right) - \left(\frac{x}{L} \right)^2 \right] \qquad (2)$$

where $\Delta T_m = \frac{RLi_{rms}^2}{8Ak_H}$ is the relevant value at mid-span, which obviously depends on the heat conductivity k_H and on the electrical resistance R of the material.

In Eq. (2), we have assumed that the temperature does not change at beam anchors, as the substrate (die) can locally compensate for the small changes caused by the current. This solution is time independent; to state it, we have accounted for the difference between the characteristic times of vibrations and heat conduction. As the beam is forced to vibrate with a frequency in the regime of kHz, the temperature rise is not allowed to accordingly vary in time during a single cycle (as the alternate current i is cosinusoidally varying in time, also ΔT_m and P are expected to display similar fluctuations). A steady-state solution is therefore considered, governed by the effective root mean square current density i_{rms} over a single period of oscillation (or loading).

To compute the related effective value of P, entering the dynamic equilibrium as stated in Eq. (1), we now exploit the additivity of the longitudinal elastic and thermal (inelastic) deformations, still valid at second-order. As the beam is axially restrained at both ends, we get:

$$P = \alpha \frac{EA}{L} \int_0^L \Delta T(x) \, \mathrm{d}x - \frac{EA}{2} \int_0^L (v')^2 \, \mathrm{d}x$$

$$= \frac{2}{3} \alpha EA \Delta T_m - \frac{EA}{2} \int_0^L (v')^2 \, \mathrm{d}x \qquad (3)$$

where α is the material coefficient of longitudinal thermal expansion. In this equation, the first term on the right hand side represents the contribution at first order (i.e. for linearized kinematics), whereas the second one is linked to the non-negligible axial stretch at second-order, which actually reduces the axial compressive deformation. According to what already discussed above, the former contribution is time-invariant; the latter one is instead continuously varying in time due to the flexural deformation of the beam.

In Eq. (3) and in the whole formulation, we have assumed that the silicon material constants, like α and E, do not depend on the temperature raise ΔT. Even if not discussed explicitly in the results Section 4, where focus is placed on relevant features of the objective functions and on the optimized geometry of the micro-beam, the analyses have reported that the small amplitudes of the excitation current i and of the earth magnetic field lead to a maximum variation of the temperature ΔT_m at the mid-span, amounting to around 20 °C at most. According to the data reported, e.g. in [10],

the corresponding variations of the silicon parameters have been therefore disregarded.

As far as the external loading term in Eq. (1) is concerned, density f for unit length stands for the overall contribution over the (constant) cross-section of the beam. By assuming gravity effects to be negligible, f is due to the Lorentz force [11]. If the system is under the action of the uniform and time-invariant earth magnetic field, of magnitude B and flowing along the out-of-plane axis z, the current i along the longitudinal axis gives rise to a lateral force density $f = iB$, which varies in time just like the current does.

To build upon Eq. (1) a reduced order model of the system, we assume now the beam to deform according to its first flexural vibration mode. Due to the nonlinear terms featured by the model under study and nested inside the buckling-driven term function of P, this assumption obviously represents an approximation. The discrepancy between the assumed deformation mode and the actual one keeps anyway small for steady-state vibrations induced by the (small amplitude) earth magnetic field; such discrepancy might also be further decreased by enhancing the model through additional, higher-order modes. Because of the clamped–clamped boundary conditions, the assumed lateral displacement v reads:

$$v(x,t) = \frac{1}{2}\left(1 - \cos\left(\frac{2\pi x}{L}\right)\right)\mathcal{V}(t) \tag{4}$$

where the variations in space and time are multiplicative decomposed, and $\mathcal{V}(t)$ represents the time history of the lateral displacement at the mid-span cross-section, the one experiencing the maximum amplitude due to the symmetry. The motion of the beam is then described by the following ordinary differential equation in the single degree-of-freedom $\mathcal{V}(t)$:

$$m\ddot{\mathcal{V}} + d\dot{\mathcal{V}} + K_1\mathcal{V} + K_3\mathcal{V}^3 = F(t) \tag{5}$$

where

$$m = \frac{3}{8}\eta L$$
$$d = 0$$
$$K_1 = \frac{2\pi^4}{L^3}EI - \frac{\pi^2}{3L}\alpha EA\Delta T_m \tag{6}$$
$$K_3 = \frac{\pi^4}{8L^3}EA$$
$$F = \frac{L}{2}iB$$

respectively represent the effective mass, damping, linear and cubic stiffness, and external load terms.

We now focus on the attached sensing plates, which are considered for simplicity to be of the same length L of the beam (see Fig. 1). These plates affect the solution by providing contributions to the mass, damping and stiffness terms of the whole system. As for the mass, the additional term simply reads:

$$m_a = 2\eta^* L \tag{7}$$

where $\eta^* = \rho A^*$, A^* being the cross-section area of each plate, which may differ from the beam one because of a different in-plane width (while the out-of-plane thickness is constant for the whole system due to technological reasons).

As for the damping due to the air surrounding the movable parts, we consider the effects arising from the interaction between the plates and the fixed, sensing electrodes. Squeeze film damping is hence the dominant source of fluid damping for this resonator, whereas drag and shear contributions are of smaller magnitude, and therefore neglected.

For a plate featuring a length L much larger than its out-of-plane thickness b, the pressure acting over the surface facing the fixed electrode reads, see e.g. [12]:

$$p(z,t) = \frac{6\mu}{g^3}\left(\frac{b^2}{4} - z^2\right)\dot{g} \tag{8}$$

where μ is the viscosity coefficient of the fluid and g is the gap between the two surfaces. This solution proves accurate for small gap values, much smaller than the surface dimensions. The resultant force acting on a single plate and resisting the beam motion is then obtained through integration as:

$$F_d = \int_{-b/2}^{b/2} p(z)L\,dz = \frac{\mu L b^3}{8g^3}\dot{g} \tag{9}$$

where edge effects close to the tips of the plate have been disregarded in view of the considered small b/L ratios. In Eq. (9), because of the geometry and of the assumed beam kinematics, $|\dot{g}| = |\dot{\mathcal{V}}|$.

Finally, let us consider the electrostatic forces resulting from the sensing system. The two massive sensing electrodes, shown in Fig. 1 as placed on the two (top and bottom) in-plane sides of the vibrating beam, are assumed to be held at a fixed potential V_0, while the beam is instead held at $V = 0$. If the plates attached to the beam do not deform while the beam itself is kept in resonance, symmetry allows modeling the sensing system as two parallel-plate capacitors. The force per unit length of the attached plates can be therefore written as:

$$f_E(\mathcal{V}) = \frac{1}{2}V_0^2\left(\frac{dC_T}{d\mathcal{V}} + \frac{dC_B}{d\mathcal{V}}\right) \tag{10}$$

where C_T and C_B are the (top and bottom) capacitances between the beam and the two aforementioned sensing electrodes, given by:

$$C_T = \frac{b}{g - \mathcal{V}}\varepsilon_0, \quad C_B = \frac{b}{g + \mathcal{V}}\varepsilon_0 \tag{11}$$

and ε_0 is the permittivity of vacuum. Accordingly, it turns out that f_E can be approximated as:

$$f_E(\mathcal{V}) \cong \frac{1}{2}V_0^2\varepsilon_0 b\left(4\frac{\mathcal{V}}{g^3} + 8\frac{\mathcal{V}^3}{g^5}\right) \tag{12}$$

where the terms in $1/(g - V)$ and $1/(g + V)$, respectively appearing in C_T and C_B, have been expanded in Taylor series about $\mathcal{V} = 0$ up to the fourth order. The two resulting terms in Eq. (12) provide, once integrated over the whole length L of the plates, additional contributions to the linear and cubic stiffness terms of Eq. (5).

Accounting for the multi-physics governing the vibration of the whole structure, the system-dependent coefficients can be recast as:

$$m = \frac{3}{8}\eta L + 2\eta^* L$$
$$d = \frac{\mu L b^3}{8g^3}$$
$$K_1 = \frac{2\pi^4}{L^3}EI - \frac{\pi^2}{3L}\alpha EA\Delta T_m - 2\frac{\varepsilon_0 bL}{g^3}V_0^2 \tag{13}$$
$$K_3 = \frac{\pi^4}{8L^3}EA - 4\frac{\varepsilon_0 bL}{g^5}V_0^2$$
$$F = \frac{L}{2}iB$$

The nonlinear dynamics of the beam, while vibrating according to its first (linear) mode, is therefore governed by relation (5), known as the Duffing equation. As detailed here above, nonlinearities are a result of the coupled electro-thermo-magneto-mechanical physics of the problem at hand.

Moving now to the optimization strategy, we assume the beam length L and the in-plane width h to be the design variables, subject to constraints of the type $L_m \leqslant L \leqslant L^M$ and $h_m \leqslant h \leqslant h^M$ where minima (L_m and h_m) and maxima (L^M and h^M) are a priori set to

avoid too stiff or too compliant (and probably excessively big) mechanical parts. L and h are optimized to achieve two goals: (i) maximizing the sensitivity to the magnetic field by maximizing the amplitude $\mathcal{V}$ of the oscillations; (ii) minimizing the power consumption by minimizing the electric resistance of the whole beam.

As for the former optimization goal, the maximum amplitude of the oscillations of the single degree-of-freedom Duffing system is provided, at varying circular frequency Ω of the forcing term F (which therefore varies in time according to $F = F_0 \cos \Omega t$), by [13]:

$$\left(\frac{F_0}{K_1}\right)^2 = \left(2\left(1-\frac{\Omega}{\omega_0}\right)\mathcal{V}_{\max} + \frac{3}{4}\frac{K_3}{K_1}\mathcal{V}_{\max}^3\right)^2 + \left(\frac{d}{m\omega_0}\mathcal{V}_{\max}\right)^2 \quad (14)$$

where $\omega_0 = \sqrt{K_1/m}$. For $\Omega = \omega_0$, the magnitude of maximum oscillation is obtained through Eq. (14) as:

$$|\mathcal{V}_{\max}| = \left[\left(\left(\frac{64F_0^4}{81k_3^4} + \frac{4096d^6k_1^6}{19683k_3^6\omega_0^6m^6}\right)^{\frac{1}{2}} + \frac{8F_0^2}{9k_3^2}\right)^{\frac{1}{3}} \right. $$
$$\left. - \frac{16d^2k_1^2}{27k_3^2\omega_0^2m^2\left(\left(\frac{64F_0^4}{81k_3^4} + \frac{4096d^6k_1^6}{19683k_3^6\omega_0^6m^6}\right)^{\frac{1}{2}} + \frac{8F_0^2}{9k_3^2}\right)^{\frac{1}{3}}}\right]^{\frac{1}{2}} \quad (15)$$

As for the latter optimization goal, as said the solution guaranteeing minimal power consumption is here considered to be directly related to a minimal electric resistance of the conductive beam. Due to the homogeneity and constant cross-section of the beam, power consumption results to be proportional to:

$$p = \frac{L}{bh} \quad (16)$$

The next section will show how a powerful topology optimizer can simultaneously account for the possibly contrasting requirements of enhancing $|\mathcal{V}_{\max}|$ and minimizing p, and for an additional constraint to keep the resonance frequency ω_0 of the beam within a pre-assigned interval.

3. Topology optimization

As we have to handle two different goals in the proposed optimization approach, the objective function is defined through a weighted sum of the functions $|\mathcal{V}_{\max}|$ and p defined in Section 2. Such functions can take values in very different intervals (potentially differing by orders of magnitude); hence, we introduce relevant normalizing (or scaling) factors $|\mathcal{V}_{\max}|_{ref}$ and p_{ref}, so as the ratios $|\mathcal{V}_{\max}|/|\mathcal{V}_{\max}|_{ref}$ and p/p_{ref} can be comparable in amplitude within the whole domain of variation for L and h. Accordingly, non-dimensional weighting factors are set as $0 \leqslant \beta_{\mathcal{V}} \leqslant 1$ and $0 \leqslant \beta_p \leqslant 1$, with the obvious constraint $\beta_{\mathcal{V}} + \beta_p = 1$.

Since the sought optimal solution has to feature maximum dynamic compliance and minimum power consumption, the optimization problem can be formally stated as:

$$\begin{cases} \min_\zeta & \varphi = -\beta_{\mathcal{V}}\frac{|\mathcal{V}_{\max}|}{|\mathcal{V}_{\max}|_{ref}} + \beta_p \frac{p}{p_{ref}} \\ \text{s.t.} & \psi_m \leqslant \psi(\zeta) \leqslant \psi^M \\ & \zeta_m \leqslant \zeta \leqslant \zeta^M \end{cases} \quad (17)$$

where $\zeta = \{L\,h\}^T$ is the vector gathering the design variables; φ is the objective function, to be minimized in order to achieve the best design; ψ represents the resonance frequency of the nonlinear beam. The two sets of constraints added to the formulation in Eq. (17) have different meanings: the one relevant to the design variables has been already discussed in Section 2, and is usually referred to as side constraints; the one relevant to the resonance frequency ψ

is instead accounted for to guarantee that every optimal solution obtained (possibly depending on $\beta_{\mathcal{V}}$ and β_p) provides a working frequency of the device compliant with manufacturer's standard, if any.

The solution of the so-called primary optimization problem (17) is generally a very difficult task, due to the computational burden tied to the evaluation of the objective function and to the relevant sensitivity analysis. This becomes a crucial issue in structural optimization problems, where φ may be a highly nonlinear function of the design variables. To overcome this, the optimization problem may be replaced with a sequence of explicit, approximate sub-problems having a simple algebraic structure of the form:

$$\begin{cases} \min_\zeta & \tilde{\varphi} \\ \text{s.t.} & \psi_m \leqslant \tilde{\psi}(\zeta) \leqslant \psi^M \\ & \zeta_m \leqslant \zeta \leqslant \zeta^M \end{cases} \quad (18)$$

where $\tilde{\varphi}$ and $\tilde{\psi}$ may be seen as Taylor expansions of φ and ψ around the current design point. The sub-problems arising in Eq. (18) can be handled through mathematical programming algorithms, like the so-called dual method [14] with the CONLIN minimizer, also exploited in the method of moving asymptotes, MMA [15].

Dual methods extensively exploit convexity and separability, features that are both peculiar to the sub-problems in Eq. (18). The convexity of the approximation ensures that the solution of the dual problem is the same solution of the original problem. The separability allows to derive an uncoupled system of equations between the primal variables and the dual unknowns, meaning that the problem can be solved independently for each primal variable. MMA provides the above features adopting a convex linearization scheme that may be regarded as a first-order Taylor series expansion in terms of the intermediate variables $1/\left(\zeta_j^U - \zeta_j\right)$ and $1/\left(\zeta_j - \zeta_j^L\right)$, where j is an index running over the component of the design variables vector. ζ_j^U and ζ_j^L are termed vertical asymptotes, and ensure that at the current iteration k one has $\zeta^L < \zeta^k < \zeta^U$. After normalization, the MMA approximation may be written as:

$$\begin{cases} \min_\zeta & \sum_{j=1}^2 \left(\frac{r_{j0}}{\zeta_j^U - \zeta_j} + \frac{s_{j0}}{\zeta_j - \zeta_j^L}\right) \\ \text{s.t.} & \Theta_m \leqslant \sum_{j=1}^2 \left(\frac{r_j}{\zeta_j^U - \zeta_j} + \frac{s_j}{\zeta_j - \zeta_j^L}\right) \leqslant \Theta^M \\ & \zeta_m \leqslant \zeta \leqslant \zeta^M \end{cases} \quad (19)$$

The above objective function calls for the computation of the values r_{j0} and s_{j0} as:

$$r_{j0} = \max\left(0, \left(\zeta_j^U - \zeta_j^k\right)^2 \frac{\partial\varphi}{\partial\zeta_j}\right)$$
$$s_{j0} = \max\left(0, -\left(\zeta_j^k - \zeta_j^L\right)^2 \frac{\partial\varphi}{\partial\zeta_j}\right) \quad (20)$$

while the constraint is written in terms of an approximated right-hand side along with analogous terms of the type:

$$r_j = \max\left(0, \left(\zeta_j^U - \zeta_j^k\right)^2 \frac{\partial\psi}{\partial\zeta_i}\right)$$
$$s_j = \max\left(0, -\left(\zeta_j^k - \zeta_j^L\right)^2 \frac{\partial\psi}{\partial\zeta_i}\right) \quad (21)$$

Once the approximated form of the constrained minimization setting has been defined, one may straightforwardly derive the Lagrange function associated to the problem, weighting also the constraint with a relevant multiplier γ. This transforms the optimization into an unconstrained problem with a new objective function $\Phi(\zeta, \gamma)$ that depends on both primal design variables ζ and dual one γ. Because of the separability property, the n-dimensional

problem can be split into n one-dimensional problems relative to each variable ζ_i. The Karush–Kuhn–Tucker conditions enforce stationarity of the Lagrange function $\Phi(\zeta, \gamma)$ with respect to ζ as necessary conditions of optimality for the constrained statements. The solution of this problem can be therefore solved explicitly for each variable, to give rise to the primal–dual relations.

MMA is ideally tailored to work with large set of unknowns, as in the optimal placement of sensors investigated in [16], and to handle equality-constrained problems, as in the herein considered setting. As shown in the next section, the iterative method searches for the optimal solution while robustly enforcing the constraints throughout the whole optimization procedure. It must be remarked that this feature is not shared by other optimization algorithms when tested on the same kind of constrained problems, like e.g. genetic approaches.

4. Results

To test the procedure here proposed, the Lorentz force microresonator of Fig. 1 has been considered. The values of the adopted physical properties of the polysilicon film constituting the sensor movable parts, and of the other geometrical, actuation and sensing parameters affecting the solution are reported in Table 1.

Side constraints on the design variables have been set as: $L_m = 100$ μm; $h_m = 2$ μm; $L^M = 1000$ μm; and $h^M = 20$ μm. Within this variable domain, the beam slenderness results to be $L/h \geqslant 5$; the optimal designs reported in what follows feature instead $L/h > 125$, which is surely enough to avoid considering shear deformations in the problem formulation. For technological reasons, the resonance frequency has been instead constrained in the domain $22 \leqslant \psi \leqslant 28$ kHz.

A first optimization has been carried out by assuming $\beta_\nu = 1$ and $\beta_p = 0$ in Eq. (17), thereby investigating the optimal design in terms of dynamic performance only. The relevant objective function φ is shown in Fig. 2: the feasible design domain, according to the handled constraints on the resonance frequency, is bounded by the lower bound (blue line) and by the upper one (black line) on ψ. The objective function displays a well-type asymptotic behavior for very slender beams, i.e. for high values of L and small values of h. According to the developed second-order theory as for the beam dynamics, such well obviously represents solutions triggering a buckled state. The adopted constraints on ψ thus help avoid the optimizer to point toward buckled configurations of the system.

A global minimum of φ is shown to arise within the considered domain for $h = 2$ μm and $L = 562.2$ μm, just along the lower bound constraint on ψ. Fig. 3 shows two-dimensional side views of the intersections between objective and constraint functions: even if only one design variable (either L or h) is shown to vary in the two graphs, it must be borne in mind that both are to be tuned so as to belong to the mentioned intersection lines. Fig. 4 shows an exemplary optimization path followed by MMA when starting from the initialization guess $h = 11$ μm and $L = 550$ μm (red dotted
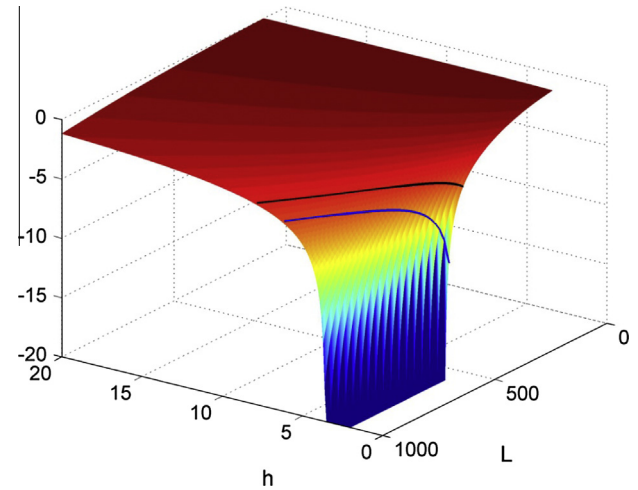

Fig. 2. $\beta_\nu = 1$, $\beta_p = 0$: objective function (beam dimensions L and h in μm); the continuous blue and black lines respectively represent its intersections with the lower bound ψ_m and the upper bound ψ^M on the resonance frequency. (For interpretation of the references to color in this figure legend, the reader is referred to the web version of this article.)

line), and also provides a comparison with the bounds on the constrained objective function. Even if moving from a point violating the prescribed constraints, the optimizer soon provides a set of
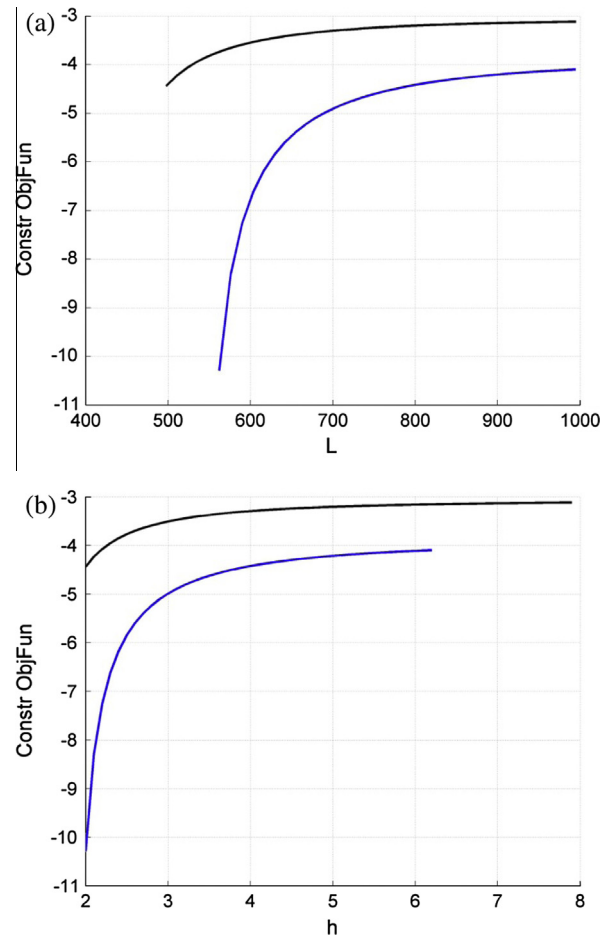

Fig. 3. $\beta_\nu = 1$, $\beta_p = 0$: side views of the intersections of the objective function with the lower bound ψ_m (blue line) and the upper bound ψ^M (black line) on the resonance frequency, at varying (a) L and (b) h. (For interpretation of the references to color in this figure legend, the reader is referred to the web version of this article.)

Table 1
Adopted values of the physical, geometrical, actuation and sensing parameters.

Property	Value
Young's modulus (GPa)	170
Thermal conductivity (W/mK)	34
Resistivity (Ωm)	3.4×10^{-5}
Thermal expansion coefficient (K^{-1})	2.5×10^{-6}
Mass density (kg/m^3)	2330
Air viscosity (Ns m^2)	6×10^{-8}
Biased voltage (V)	2
Gap (m)	2×10^{-6}
Excitation current (mA)	1
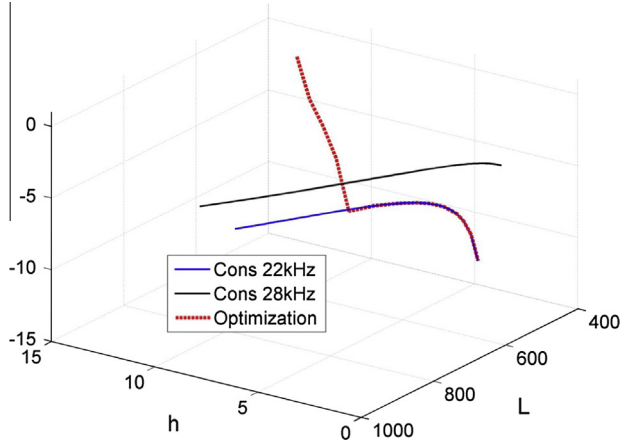
Fig. 4. $\beta_v = 1$, $\beta_p = 0$: optimal path followed by the minimization algorithm (red dotted line), and intersections of the objective function with bounds ψ_m (blue line) and ψ^M (black line) on the resonance frequency. (For interpretation of the references to color in this figure legend, the reader is referred to the web version of this article.)
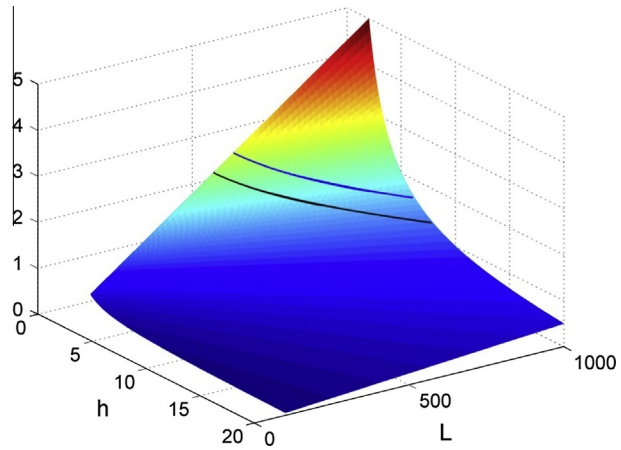

Fig. 5. $\beta_v = 0$, $\beta_p = 1$: objective function; like in Fig. 2, the continuous blue and black lines respectively represent the intersections with the lower bound ψ_m and the upper bound ψ^M on the resonance frequency. (For interpretation of the references to color in this figure legend, the reader is referred to the web version of this article.)

feasible solutions to the arising sub-problems (see Section 3), and finally attains the global minimum as expected.

A second run of the optimizer has been performed by assuming $\beta_v = 0$ and $\beta_p = 1$, so as to assess the effect of the power consumption issue. The relevant objective function is reported in Fig. 5: it can be neatly seen that an optimal solution to this problem can be far from the one obtained for the compliance goal. A global minimum is shown to arise at $h = 7.9$ μm and $L = 1000$ μm, just along the upper bound on ψ. As before, Fig. 6 shows two-dimensional side views of the intersections of the objective function with the bounds. According to Eq. (16), it results that the optimal solutions are now characterized by the maximum allowable values of the beam width h. Fig. 7 compares the bounds on the constrained objective function with the optimization path followed by MMA, when departing from the same initialization guess of the former case (red dotted line). Once again, the optimizer provides a set of feasible solutions to the arising sub-problems, and ends the analysis at the global minimum of φ.

The above investigations allow highlighting that the two partial objective functions $-\frac{|V_{max}|}{|V_{max}|_{ref}}$ and $\frac{p}{p_{ref}}$ provide different optimal
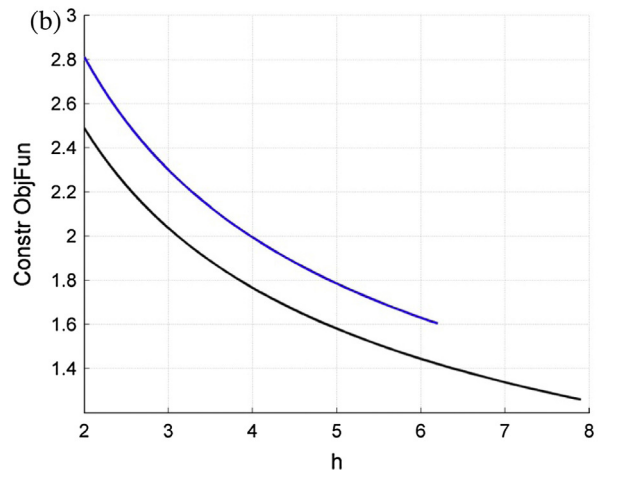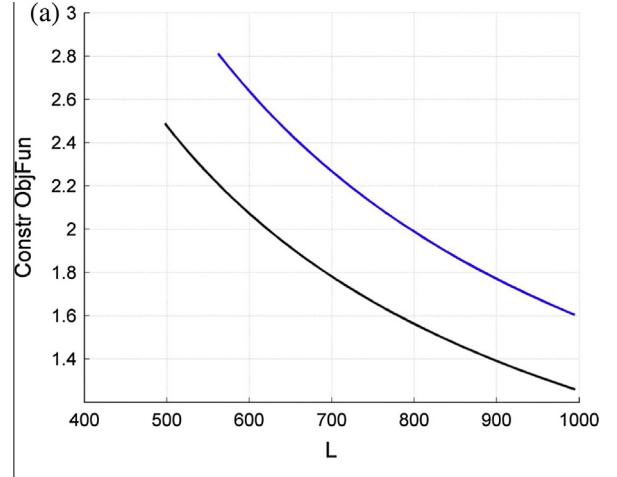

Fig. 6. $\beta_v = 0$, $\beta_p = 1$: side views of the intersections of the objective function with the lower bound ψ_m (blue line) and the upper bound ψ^M (black line) on the resonance frequency, at varying (a) L and (b) h. (For interpretation of the references to color in this figure legend, the reader is referred to the web version of this article.)
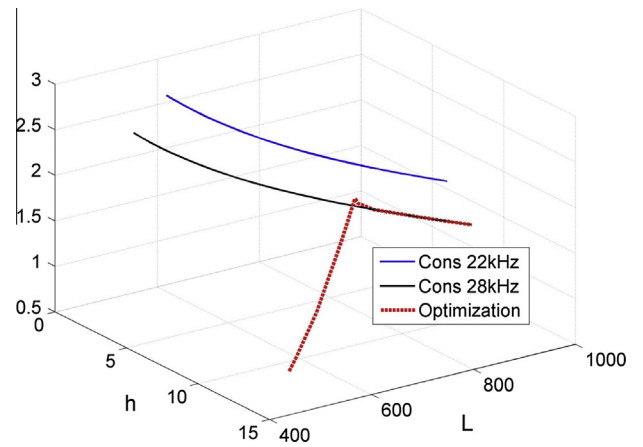

Fig. 7. $\beta_v = 0$, $\beta_p = 1$: optimal path followed by the minimization algorithm (red dotted line), and intersections of the objective function with bounds ψ_m (blue line) and ψ^M (black line) on the resonance frequency. (For interpretation of the references to color in this figure legend, the reader is referred to the web version of this article.)

solutions, within the feasible range prescribed for the unknowns. Anyhow, in both cases the optimal solution has been found to lie along one of the frequency constraints.
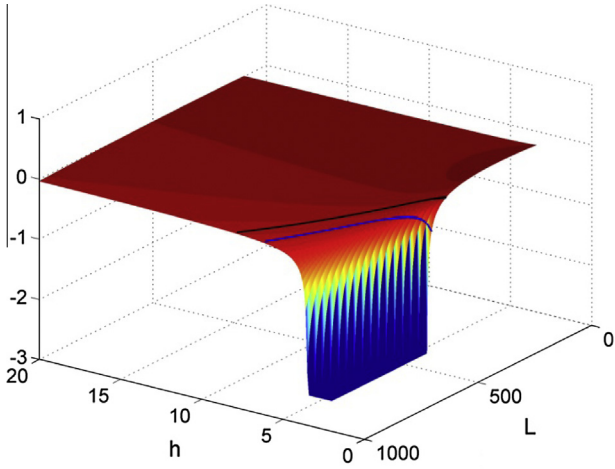
Fig. 8. $\beta_\nu = 0.85$, $\beta_p = 0.15$: objective function, and intersections with bounds ψ_m (blue line) and ψ^M (black line) on the resonance frequency. (For interpretation of the references to color in this figure legend, the reader is referred to the web version of this article.)
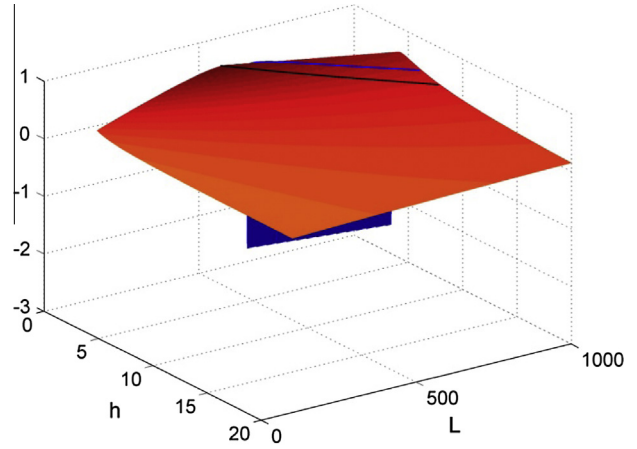

Fig. 10. $\beta_\nu = \beta_p = 0.5$: objective function, and intersections with bounds ψ_m (blue line) and ψ^M (black line) on the resonance frequency. (For interpretation of the references to color in this figure legend, the reader is referred to the web version of this article.)
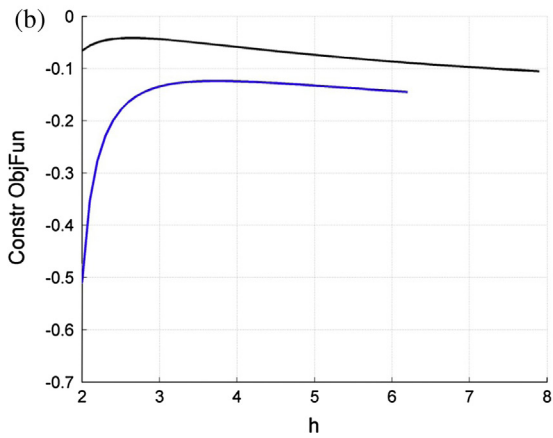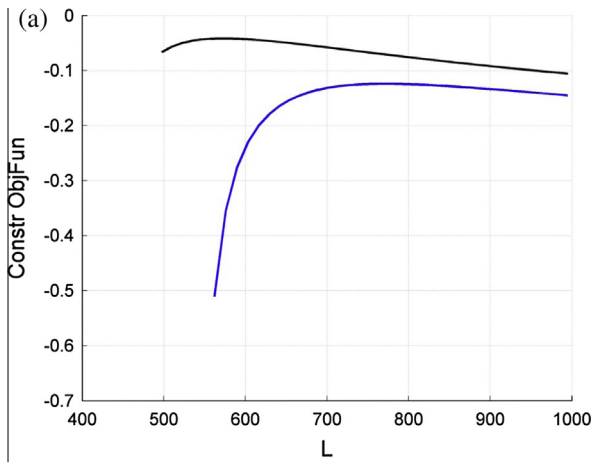

Fig. 9. $\beta_\nu = 0.85$, $\beta_p = 0.15$: side views of the intersections of the objective function with the lower bound ψ_m (blue line) and the upper bound ψ^M (black line) on the resonance frequency, at varying (a) L and (b) h. (For interpretation of the references to color in this figure legend, the reader is referred to the web version of this article.)
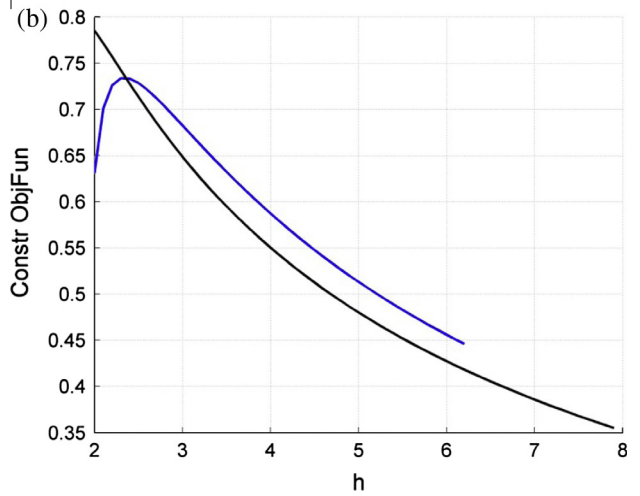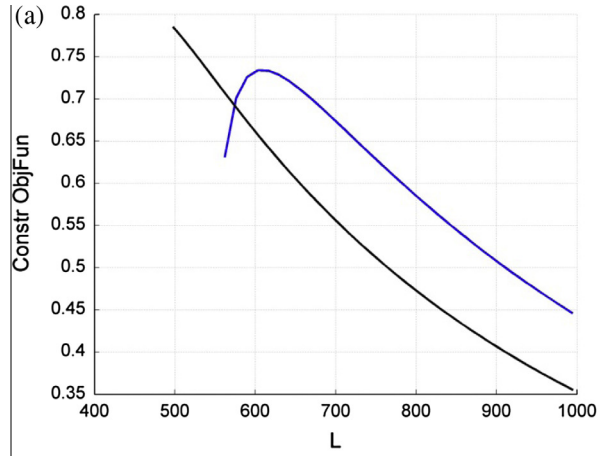
Fig. 11. $\beta_\nu = \beta_p = 0.5$: side views of the intersections of the objective function with the lower bound ψ_m (blue line) and the upper bound ψ^M (black line) on the resonance frequency, at varying (a) L and (b) h. (For interpretation of the references to color in this figure legend, the reader is referred to the web version of this article.)

Even if located along the constraints on φ, the optimal solutions depend on the adopted values of the weighting factors β_v and β_p. This is clearly shown in Figs. 8–10, reporting the objective function and its intersections with the constraints on ψ, for two different weight sets: $\beta_v = 0.85$, $\beta_p = 0.15$; and $\beta_v = \beta_p = 0.5$. Weights can move the optimal solution from one end of the available range for the parameters (see Fig. 9), to the opposite one (see Fig. 11). Hence, it can be concluded that the choice of the weights in the objective function is crucial in a design phase, when importance is given to optimization goals contrasting in terms of results.

The strategy herein adopted to cope with the multi-objective optimization leaves the freedom to choose a suitable set of weights based on (formerly achieved) know-how of the dependence of each constrained objective function on the parameters, see Figs. 2 and 5. Alternatively, the optimizer could be adopted to generate sets of optimal solutions with the aim of computing an approximation of the entire Pareto front, i.e. the whole set of parameters for which neither of the objective functions can be decreased unless the other one is increased. This latter approach is of course more expensive in terms of computational time, since it requires an increased number of runs; the other way around, it could be conveniently adopted in more complex cases for which the choice of a suitable set of weights is not straightforward.

5. Conclusions

In this paper, a topology optimization technique has been adopted to design a Lorentz-force MEMS magnetometer. The results have shown that topology optimization techniques can be applied also in a multi-physics context, like the one here handled for the modeling of a beam vibrating under the action of Lorentz force, Joule-related thermal effects (possibly inducing buckling) and electrostatic loading.

Work in progress concerns the practical exploitation of topology optimization potentialities for the design of commercial MEMS magnetometers. New magnetometers have been re-designed taking into consideration the results discussed in the present paper, the behavior of the new devices will be discussed in a future publication after completing the fabrication process and obtaining experimental data.

References

[1] Ren D, Wu L, Yan M, Cui M, You Z, Hu M. Design and analyses of a MEMS based resonant magnetometer. Sensors 2009;9:6951–66.
[2] Thompson MJ, Li M, Horsley DA. Low power 3-axis Lorentz force navigation magnetometer. In: Proc IEEE MEMS, January 23–27, 2011.
[3] Li M, Rouf VT, Thompson J, Horsley D. Three-axis Lorentz-force magnetic sensor for electronic compass applications. J Microelectromech Syst 2012;21:1002–10.
[4] Rochus V, Jansen R, Rottenberg X, Tilmans HAC, Ranvier S, Lamy H, et al. Comparison of Ni- and SiGe-based MEMS magnetometers. In: Proc Eurosime 12, Lisbona, 16–18 April, 2012.
[5] Langfelder G, Buffa C, Tocchio A, Frangi A, Longoni A, Lasalandra E. Design criteria for MEMS magnetometers resonating in free-molecule flow and out of the acoustic bandwidth. In: Proc 2012 IEEE international frequency control symposium, IFCS 2012; 2012. p. 818–22.
[6] Chen L, Wang W, Li Z, Zhu W. Stationary response of Duffing oscillator with hardening stiffness and fractional derivative. Int J Non-Linear Mech 2013;48:44–50.
[7] Ardito R, Comi C, Corigliano A, Frangi A. Solid damping in micro electro mechanical systems. Meccanica 2008;43:419–28.
[8] Shih YS, Wu GY, Chen EJS. Transient vibrations of a simply-supported beam with axial loads and transverse magnetic fields. Mech Struct Mach 1998;26:115–30.
[9] Xi X, Yang Z, Meng L, Zhu C. Primary resonance of the current-carrying beam in thermal-magneto-elasticity field. Appl Mech Mater 2010;29–32:16–21.
[10] Hull R, editor. Properties of crystalline silicon. London (UK): Institution of Electrical Engineers; 1999.
[11] Han JS, Ko JS, Korvink JG. Structural optimization of a large-displacement electromagnetic Lorentz force microactuator for optical switching applications. J Micromech Microeng 2004;14:1585–96.
[12] Bao M, Yang H. Squeeze film air damping in MEMS. Sens Actuat A 2007;136:3–27.
[13] Comi C, Corigliano A, Langfelder G, Longoni A, Tocchio A, Simoni B. A resonant microaccelerometer with high sensitivity operating in an oscillating circuit. J Microelectromech Syst 2010;19:1140–52.
[14] Fleury C. Structural weight optimization by dual methods of convex programming. Int J Numer Methods Eng 1979;14:1761–83.
[15] Svanberg K. Method of moving asymptotes: a new method for structural optimization. Int J Numer Methods Eng 1987;24:359–73.
[16] Bruggi M, Mariani S. Optimization of sensor placement to detect damage in flexible plates. Eng Optim 2013;45:659–76.